

# Sputtered AlN Thin Films for Piezoelectric MEMS Devices - FBAR Resonators and Accelerometers

\*Friedel Gerfers<sup>1</sup>, Peter M. Kohlstadt<sup>1</sup>, Eyal Ginsburg<sup>1</sup>, Ming Yuan He<sup>1</sup>,  
Dean Samara-Rubio<sup>1</sup>, Yiannos Manoli<sup>2</sup> and Li-Peng Wang<sup>1</sup>

<sup>1</sup>Intel Corporation, Microsystems Technology, Santa Clara

<sup>2</sup>Albert-Ludwigs University Freiburg

<sup>1</sup>USA

<sup>2</sup>Germany

## 1. Introduction

Over the past two decades, significant advances have been made in the field of micromachined sensors and actuators. As microelectromechanical systems (MEMS) have become mainstream, a clear need for the integration of materials other than silicon and its compounds into micromachined transducers has emerged. MEMS devices based on piezoelectric materials take advantage of the high energy transduction that scales very favorably upon miniaturization leading to an ever-growing interest in piezoelectric films for MEMS applications.

Piezoelectric materials provide a direct transduction mechanism to convert signals from mechanical to electrical domains and vice versa. The reversible and linear piezoelectric effect manifests as the production of a charge (voltage) upon application of stress (direct effect) and/or as the production of strain (stress) upon application of an electric field (converse effect). Transducers using piezoelectric materials can be configured either as actuators, when the design of the device is optimized for generating strain or stress using the converse piezoelectric effect, or as sensors when the design of the device is optimized for the generation of an electric signal, using direct piezoelectric effect, in response to mechanical input. Furthermore, piezoelectric devices also allow the integration of sensing and actuating elements in one device (Xu et al., 2002). The elementary piezoelectric effects are given by

$$D_i = d_{ij}\sigma_j + \epsilon_{ii}^T E_i \quad \text{or} \quad D_i = e_{ij}S_j + \epsilon_{ii}^S E_i \quad (1)$$

$$S_j = s_{ij}^E \sigma_j + d_{ij} E_i \quad \text{or} \quad T_j = c_{ij}^E S_j - e_{ij} E_i \quad (2)$$

---

\* Friedel Gerfers was with Intel Corporation, Microsystems Technology, Santa Clara, USA. He is now with Aquantia Inc., USA. Peter M. Kohlstadt is now with Solyndra Inc., USA. Li-Peng Wang is now with Technologies Inc., USA.

where  $S_j$  is the mechanical strain,  $\sigma_j$  is the mechanical stress,  $E_i$  is the electric field,  $D_i$  is the electrical displacement,  $c_{ij}$  is the elastic stiffness constant,  $s_{ij}$  is the elastic compliance coefficient, and  $\varepsilon_{ij}$  is the permittivity. The piezoelectric coefficients,  $d_{ij}$  and  $e_{ij}$ , are third rank tensors which in reduced tensor notation correspond to a  $3 \times 6$  matrix (Nye, 1995; Giacomazzo, 2002).

Furthermore, the indices ( $i = 1 \dots 3$ ) define normal electric field or displacement orientation, ( $j = 1 \dots 3$ ) define normal mechanical stresses or strains and ( $j = 4 \dots 6$ ) represent shear strains or stresses.

In the direct effect using equation (1), a mechanical stress  $\sigma_j$  or strain  $S_j$  causes a net electrical displacement,  $D_i$ , on  $i$  faces of the material, the magnitude of which depends on  $d_{ij}$  and  $e_{ij}$  respectively. Similarly, the converse effect expressed by equation (2) relates the induced normal and shear stress or strain to the applied electric field via the piezoelectric coefficient tensor. As a result, large piezoelectric coefficients  $d_{ij}$  are desired in actuator applications whereas sensor applications take advantage of large  $e_{ij}$  coefficients.

The piezoelectric coefficients are not the only material parameters of interest. In resonant structures the electromechanical coupling coefficient (3) and the dielectric loss angle ( $\tan\delta$ ) (4) are essential measures in piezoelectric materials. The coupling coefficient represents the effectiveness of the energy transformation from the mechanical (electrical) to the input electrical (mechanical) energy. The definition of coupling coefficient depends on the orientation. The planar coupling coefficient,  $k_p$ , describes the radial coupling in a thin disc, when the electrical field is applied through the thickness, whereas the thickness coupling coefficient,  $k_t$ , is identical to  $k_{33}$  when the element is clamped laterally.

$$k_t^2 = \frac{d_{33}^2}{\varepsilon_{33}^T S_{33}^E} \quad (3)$$

$$\tan\delta = \omega C \times R \quad (4)$$

Part of the electrical energy is dissipated and transformed to heat. The dielectric loss angle  $\tan\delta$  (4) (the inverse denotes the dissipation factor  $\eta$ ) quantifies this phenomenon. The term refers to the angle in a complex plane between the resistive (lossy) component ( $R$ ) of an electromagnetic field and its reactive (lossless) component ( $C$ ). The resistive component in (4) generates also a noise current or voltage, which limits directly the signal-to-noise ratio of the sensors.

$$SNR = \frac{e_{31}^2}{\sqrt{\varepsilon_0 \varepsilon_{33} \tan\delta}} \quad (5)$$

Among the piezoelectric films used, Aluminum Nitride (AlN) films have been less explored than Lead zirconate titanate (PZT) and Zinc oxide (ZnO) films due to its smaller piezoelectric constant. However, its temperature/humidity stability (Lakin et al., 2000), higher signal-to-noise ratio (Trolrier-McKinstry & Murali, 2004; Setter, 2005) and the compatibility with CMOS processing are attractive (Gerfers et al., 2006; Oestman et al., 2006). Furthermore, AlN is a large band gap material (6eV) with a large resistivity, whereas ZnO is really a semiconductor (3eV) with the inherent risk of increased conductivity due to off-stoichiometry. This low DC resistivity translates into a high dielectric loss at low frequencies, which is specially harmful for sensor and actors operating at frequencies below 10kHz (Setter, 2005).

Two types of piezoelectric MEMS devices, surface-micromachined piezoelectric resonators and bulk-micromachined accelerometers, which utilize longitudinal ( $d_{33}$  mode) and transverse ( $d_{31}$  mode) piezoelectric effects, will be presented in this chapter. Film bulk acoustic resonator (FBAR) resonators have proven advantages of low loss, high power handling, small form factor, and easy silicon integration compared to conventional ceramic and surface acoustic wave (SAW) structures (Ruby et al., 2001; Weigel et al., 2002). Thus, FBAR resonators are getting popular as a transmitter and/or receiver filters e.g. in GSM/CDMA/UMTS applications (Ruby & Merchant, 1994; Ueda et al., 2005), replacing the bulky SAW filters.

For the reconfigurable RF front ends, the integration of adjacent-band filters in one chip is attractive from the cost and form factor perspective. But the resonance frequency of a FBAR is determined by the thickness of the film stack, which is equal to the corresponding half wavelength of the first fundamental mode (Wang et al., 2006). However, it is impractical from a manufacturing perspective to have multiple thicknesses of film stacks in order to obtain multiple-frequency resonators/filters. Therefore, we propose in this chapter a solution for this shortcoming (Wang et al., 2006).

Piezoelectric MEMS accelerometers have been successfully used in many applications, such as automotive, mobile phones, consumer electronics, and aerospace. An advanced application of condition-based maintenance (CBM) in equipment vibration monitoring and diagnostics is still solely relying on conventional bulk piezoelectric transducers due to the stringent dynamic range requirements. In recent years, CBM systems have naturally progressed from traditional data collector and wired systems to wireless sensor networks due to lower cost and ease of use (McLean & Wolfe, 2002). As a result, availability of high-performance, low-cost, and small form factor vibration sensors become a limiting factor to proliferate the number of monitoring points. Bulk-micromachined accelerometers (Gerfers et al., 2006) offer an appealing solution for such applications providing several benefits over conventional capacitive accelerometers (Monajemi & Ayazi, 2006; Kulah et al., 2006) in terms of form factor and noise. AlN based accelerometers provide an inherently small dissipation factor (around 0.1%) resulting in an excellent low frequency noise performance (Setter, 2005). Based on the initial sensor design (Gerfers et al., 2006), this chapter introduces the technique of stress concentration to improve the overall accelerometer SNR (Gerfers et al., 2007). In the first section, the deposition of highly *c*-axis oriented AlN films is described, since optimal piezoelectric and crystal properties of AlN films are essential for devices' performance (Ruby & Merchant, 1994; Naik et al., 2000). Furthermore, Section 2 discusses processing details and experimental results of the sputtered piezoelectric AlN films. The design of AlN surface-micromachined piezoelectric resonators, its fabrication and experimental results is presented in Section 4. Based on these FBAR resonators an on-chip tuning mechanism is proposed in Section 5, in order to obtain a multiple-frequency resonator (filter) in a single device.

Next, the design and characterization of low noise AlN based accelerometers is presented. Section 7 introduces the technique of stress concentration for ultra low noise piezoelectric AlN accelerometers. Experimental results demonstrate the SNR improvements. Finally, concluding remarks complete this chapter.

## 2. Piezoelectric AlN films

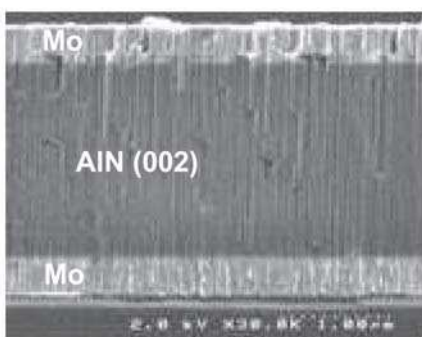
Both, surface-micromachined piezoelectric resonators and bulk-micromachined accelerometers require thin piezoelectric layers in the order of a few  $\mu\text{m}$  (Loebl et al., 1999;

Xu et al., 2002). Attractive piezoelectric films are beside aluminum nitride (AlN) (Wang et al., 2006), ZnO and  $\text{PbZr}_x\text{Ti}_{1-x}\text{O}_3$  (PZT) (Loebl et al., 1999). With AlN films, electromechanical coupling coefficients  $k_t^2$  of  $> 6\%$  and low losses can be achieved, if strongly c-axis oriented AlN films are grown (Loebl et al., 1999; Wang et al., 2006).

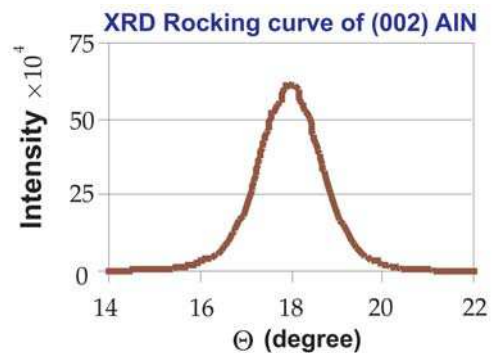
To achieve high piezoelectric coupling in AlN layers, they have to be strongly oriented in (002) direction (Loebl et al., 1999; Wang et al., 2006). Therefore, columnar AlN grains with the c-axis perpendicular to the substrate are needed. The texture of sputtered AlN films depends on the sputter deposition conditions, on the substrate, and on the deposition temperature. Also the AlN layer thickness has an influence on the quality and orientation of the grains. The formerly mentioned effects of substrate temperature, substrate and AlN layer thickness are investigated in detail in (Loebl et al., 1999).

The used AlN films were prepared by reactive sputtering (Wang et al., 2006), a technique with advantages of low deposition temperature, easy process control and low cost when compared to alternatives such as metal-organic chemical vapor deposition (MOCVD) and molecular beam epitaxy (MBE). The AlN films were sputtered at various conditions - substrate temperature from room temperature to  $300^\circ\text{C}$ ,  $\text{N}_2/\text{Ar}$  gas ratio of 9 to 1, pressure of 1 to  $6\text{mTorr}$ , and power of 1 to  $4\text{kW}$  - to obtain optimized films' properties. X-ray diffraction (XRD) rocking curve analysis was used to characterize the sputtered films since it has been shown that there is a correlation between the full width at half maximum (FWHM) of the XRD rocking curve and piezoelectric properties (Naik et al., 2000; Liaw & Hickernell, 1995). Fig. 1(a) shows an AlN film sample, prepared at optimized conditions, have desirable c-axis textured crystalline structure. The XRD rocking curve in Fig. 1(b) also shows the FWHM of (002) AlN as low as  $1.57^\circ$ .

The performance characteristics of the AlN devices, such as insertion loss, effective coupling coefficient, and the quality factor are highly related to the quality of both the piezoelectric and electrode materials (Ueda et al., 2005). In this work, Molybdenum (Mo) has been used as an electrode material due to its low resistivity and high acoustic impedance. Beyond, the quality of AlN films is affected by the surface roughness of the underlying film (Ueda et al., 2005).



(a) SEM micrograph

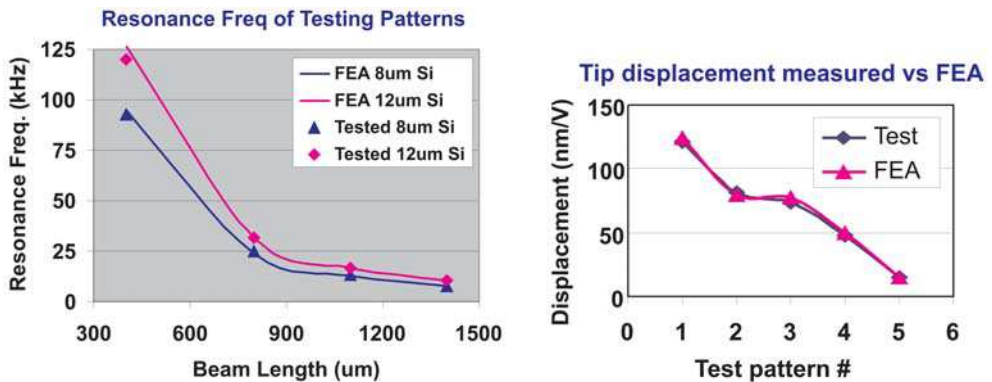


(b) AlN XRD rocking curve

Fig. 1. (a) SEM micrograph of highly c-axis textured AlN films; (b) (002) AlN XRD rocking curve with FWHM of  $1.57^\circ$ .

### 3. Material properties of sputtered polycrystalline AlN thin films

Since material properties of sputtered polycrystalline AlN films can vary over a wide range depending on the deposition conditions, it's important to characterize elastic and piezoelectric properties of the AlN films for future design and simulation. Phase velocity in the longitudinal direction (therefore,  $c_{33}$ ) and  $e_{33}$ , were extracted from measured resonance frequencies and  $k_t^2$  of the resonators with different thickness. To obtain transverse properties, various cantilever-beam test patterns were fabricated in the same chip of the accelerometers. Impedance resonance measurements were performed to obtain resonance frequencies of the beams and these were fit to FEA values to extract the stiffness matrix of the AlN films (see Fig. 2(a)). The transverse piezoelectric constant,  $e_{31}$ , was determined by measuring mechanical response (velocity) to an electrical drive signal using a laser vibrometer. Good matching between experimental and FEA results for all testing patterns were shown in Fig. 2(a)-(b). The extracted material parameters are given in Table. 1.



(a) Measured resonance frequencies

(b) Transverse piezoelectric constant

Fig. 2. (a) Measured resonance frequencies of all cantilever beams fit well with FEA-simulated values. (b) Transverse piezoelectric constant ( $e_{31}$ ) was extracted by fitting measured and FEA-simulated values.

Materials	Materials Properties
Mo (sputtered)	$E = 503GPa, \nu = 0.33,$ $\rho = 7000kg/m^3$
AlN (elastic properties)	$c_{11} = 375GPa, c_{12} = 125GPa,$ $c_{13} = 120GPa, c_{33} = 435GPa,$ $c_{44} = 118GPa, \rho = 2700kg/m^3$
AlN (piezoelectric properties)	$e_{31} = -0.58C/m^2,$ $e_{33} = 1.55C/m^2,$ $e_{15} = -0.48C/m^2$

Table 1. Summary of the extracted properties of piezoelectric film stack.

## 4. Piezoelectric resonators

The basic FBAR resonator structure is a piezoelectric film sandwiched between two electrode films, as shown in Fig. 1(a). The fabrication process flow of such an AlN piezoelectric resonator is shown in Fig. 3. The substrates were 6-in diameter (100) silicon wafers. The process started with a silicon trench etch, followed by trench fill using silicon dioxide as a sacrificial layer. The surface was then planarized by a chemical-mechanical polishing (CMP) step. It is important to have a very smooth surface for the following piezoelectric film stack deposition. A bottom Mo layer ( $0.32\mu\text{m}$ ) was sputtered and patterned to define the electrode area. An AlN layer ( $1.1\mu\text{m}$ ) was deposited by reactive sputtering. A second Mo layer was deposited and patterned to define top electrode area. The AlN layer was dry etched to open contact windows on bottom Mo electrodes and form release holes. Finally, the sacrificial layer was etched with BOE to release the membrane. Fig. 4(a) shows optical and (b) cross-section SEM micrographs of a resonator after completion of the fabrication.

### 4.1 Experimental results

The resonators were tested using an Agilent network analyzer. One-port S-parameters were measured to obtain the input impedance of the resonators, shown in Fig. 4(c). Then Butterworth-Van Dyke equivalent circuit was used to extract resonator's quality factor, series/parallel resonant frequency and effective coupling coefficient. For the 2GHz resonator, a  $Q$  as high as 1000 and  $k_t^2$  of 6.5% were achieved.

In addition to the Mo electrodes, resonators with CMOS-compatible Al electrodes were investigated. However, a lower  $Q$  (3 times worse) was found due to a higher acoustic propagation loss of Al (see Fig. 4(d)). This result was confirmed in (Ueda et al., 2005).

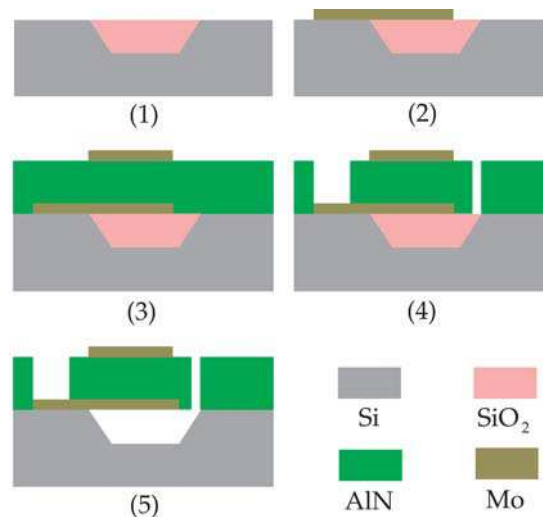


Fig. 3. Fabrication process flow of AlN piezoelectric resonators

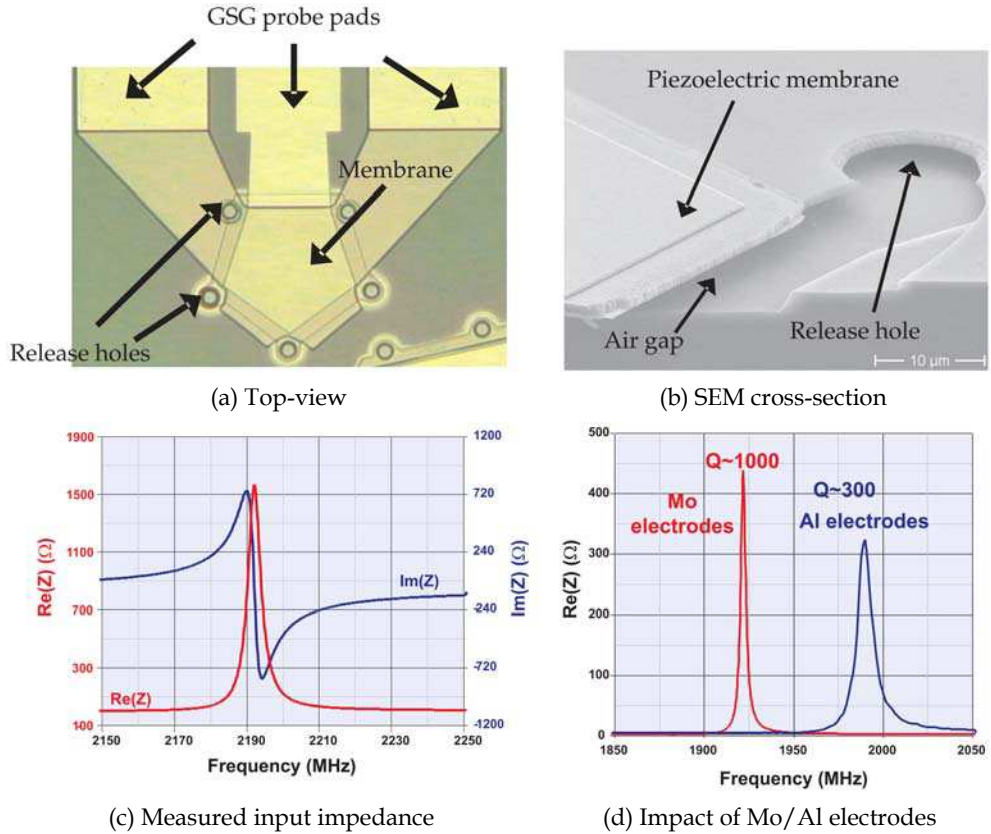


Fig. 4. Surface-micromachined AlN piezoelectric resonator, (a) top-view optical graph, (b) cross-section SEM graph. (c) Measured input impedance of the 2GHz resonator achieving a Q of 1000 and  $k_t^2$  of 6.5%; (d) Resonators with Mo electrodes have higher Q than the ones with Al electrodes.

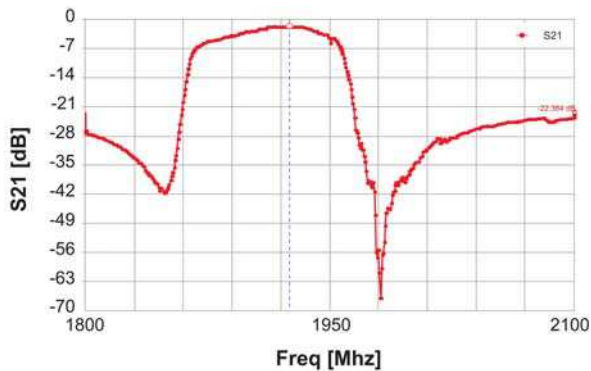


Fig. 5. Measured frequency response of the FBAR filter.

The measured frequency response of the FBAR filter is shown in Fig. 5. The insertion loss is  $1.7\text{dB}$  and the lower and upper stopband rejection is  $27\text{dB}$  and  $23\text{dB}$  respectively.

## 5. Method of fabricating multi-frequency film FBAR in a single chip

The resonance frequency of a FBAR is determined by the thickness of the film stack, which is equal to the corresponding half-wavelength of the first fundamental mode (Lakin et al., 1995). However, it is impractical from a manufacturing perspective to have multiple thicknesses of film stacks in order to obtain multiple-frequency resonators/filters. In (Piazza et al., 2005) the authors explore AlN piezoelectric resonators operating in contour modes with resonance frequencies determined by in-plane dimensions. A much lower electromechanical coupling coefficient, which is a key parameter for the use of FBARs as a front-end RF filter, was obtained. In the following we describe an approach for integrating multiple-frequency FBARs in a single chip (Huang et al., 2005; Wang et al., 2006). The presented experimental results verify the novel concept and show the performance of the modified FBARs.

Two main configurations, air-gap FBAR and solidly mounted resonator (SMR), have been used to create low acoustic impedance terminations; therefore, the acoustic energy is confined within the piezoelectric film stack, which is critical for achieving a high mechanical quality factor  $Q$ . The air-gap FBAR has the piezoelectric film stack suspended with air on both sides. On the other hand, the SMR has an air interface on the free surface side and a quarter-wavelength acoustic mirror on the substrate side. In this work, only air-gap FBARs were used to demonstrate the concept, which should also be applicable to SMR FBARs (Wang et al., 2006).

The key concept of the frequency tuning is based on the mass loading effect. An additional tuning layer was added on top of the conventional FBAR membrane, Mo/AlN/Mo film stack. Then the tuning layer was patterned with a pitch of  $S$  and width of  $L$ . A schematic of the modified FBAR is shown in Fig. 6(a). Therefore, different mass loading (different  $L/S$  ratios) effects can be obtained by controlling the width and the pitch of the tuning patterns. The trimming Mo layer was patterned using different photomasks to define loading patterns. Figure 6(b) shows a SEM micrograph of a modified FBAR after completion of the fabrication.

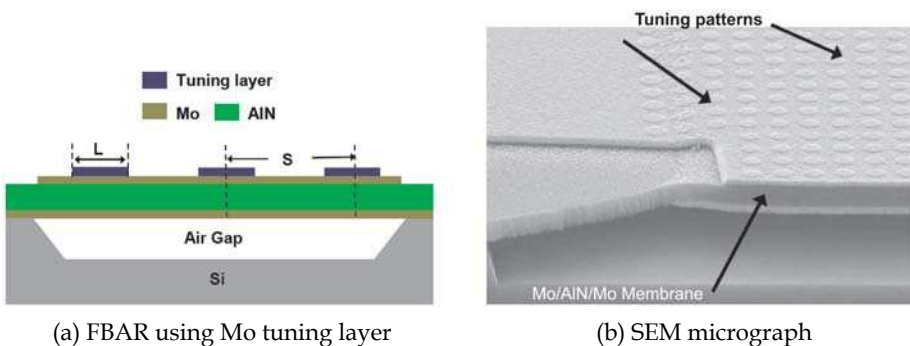


Fig. 6. (a) Schematic of a modified FBAR - a tuning layer (Mo) is added and patterned on top of a conventional FBAR. (b) SEM micrograph of a released FBAR membrane, showing a Mo tuning layer that was deposited and patterned on top of the membrane.

### 5.1 Experimental results

Both, the series resonance frequency ( $f_s$ ) and parallel resonant frequency ( $f_p$ ) were analyzed from the one-port S-parameter measurements. The  $k_t^2$  was calculated using

$$k_t = \frac{\pi}{2} \sqrt{1 - \frac{f_s}{f_p}}. \quad (6)$$

The comparison of different loading FBARs was made on the same die to minimize the frequency variation caused by the thickness variation of the deposited films (typically < 0.2% within die variation). When the pitch of tuning patterns ( $40\mu\text{m}$ ) was much larger than the membrane thickness ( $1.8\mu\text{m}$ ), two distinct resonant peaks were measured (Wang et al., 2006). The lower-frequency peak corresponded to the thickness mode with the tuning pattern and the higher-frequency one corresponded to the thickness mode without the tuning layer. The two resonant peaks agreed with the prediction from the finite element analysis, where stress-contours reveal two distinct resonant modes at the corresponding frequencies.

To achieve a desirable frequency response, the tuning patterns with  $1.5\mu\text{m}$  pitch and five different loading percentages, 0, 20, 42, 64, and 100%, were designed and fabricated. The tested results, shown in Fig. 7, demonstrate that the resonant frequencies were modulated in relation to the corresponding loading percentages. More importantly, the modulated resonance peaks maintain the same shape as the non-modulated one; that is, a pure frequency shift was achieved. Three different thicknesses of tuning layers (75, 100, and  $150\text{nm}$  Mo) were fabricated to study total tuning ranges and sensitivities (Wang et al., 2006). The results demonstrate that the thicker tuning layer provides, as expected, a larger loading effect and a wider total tuning range. For all modified FBARs, the effective coupling coefficient,  $k_t^2$ , was maintained within 90% of the non-modified one.

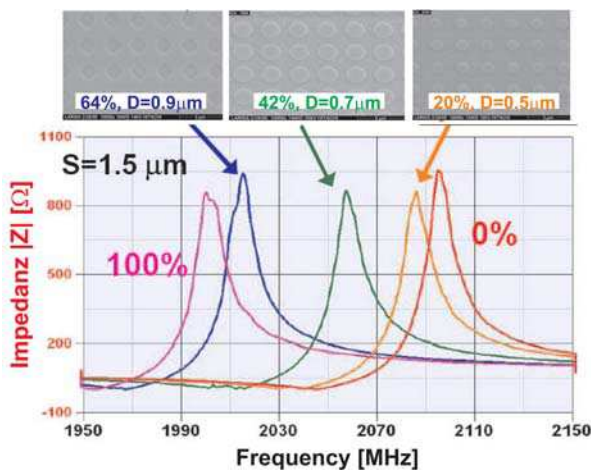


Fig. 7. Resonance frequencies were modulated according to the loading percentages. The resonant peaks of modified FBARs maintain a desirable response, a pure frequency shift, when the pitch ( $S = 1.5\mu\text{m}$ ) is smaller than the membrane thickness ( $1.8\mu\text{m}$ ).

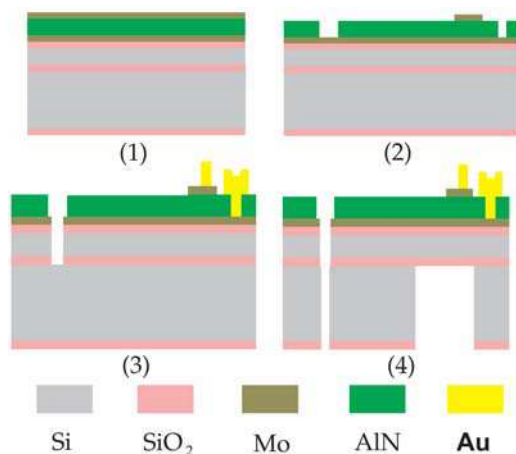


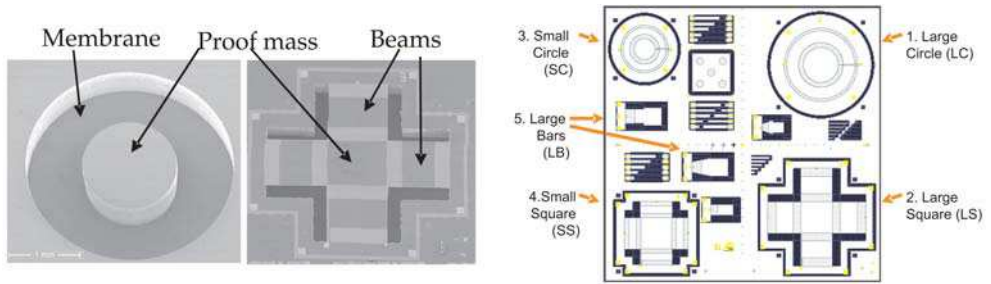
Fig. 8. Process flow of bulk micromachined piezoelectric AlN accelerometer using SOI wafer.

## 6. Bulk-micromaschined accelerometers

MEMS accelerometers using piezoelectric AlN thin film as read-out have been attracting a great deal of attention due to their simple structure, high SNR, small dielectric loss angle ( $\tan\delta$ ), temperature/humidity stability and compatibility with CMOS processing (Lakin et al., 2000; Trolier-McKinstry & Murali, 2004; Wang et al., 2006; Gerfers et al., 2007). The fabrication process of AlN piezoelectric accelerometers is based on bulk micromachining and silicon on insulator (SOI) techniques in order to have a large proof mass for low noise floor as well as precise device thickness control for minimal performance variation. The fabrication process flow is outlined in Fig. 8. First, piezoelectric films stack ( $0.25\mu\text{m Mo} / 1.5\mu\text{m AlN} / 0.25\mu\text{m Mo}$ ) was deposited on 6" silicon-on-insulator (SOI) wafers which have active Si thickness of  $7.75\mu\text{m}$  and  $12.09\mu\text{m}$ ,  $2\mu\text{m}$  buried SiO<sub>2</sub>, and  $600\mu\text{m}$  bulk Si (shown in Fig. 8-(1)). Then the top Mo layer was patterned to define the electrode area and followed by AlN patterning to open contact windows on bottom Mo electrodes (see Fig. 8-(2)). The film stack of bottom Mo, oxide and active Si as well as buried oxide was etched to define flexible sensing structures of different accelerometer designs - cantilever beams, clamp-clamp beams, and annular membranes. The final front-side process was electroplating  $3\mu\text{m Au}$  on the contact area (see Fig. 8 (3)). Finally, the wafers were completed with the backside process of DRIE  $600\mu\text{m}$  bulk Si to release the accelerometers. Fig. 9(a) shows SEM graphs of two initial accelerometer designs, an annular membrane and a clamp-clamp beams after completion of the fabrication.

### 6.1 PE accelerometer testing

The differential accelerometer designs were epoxied and wire-bonded to a special printed circuit boards (PCB), such that the proof masses are free to move (Gerfers et al., 2006). This sensor PCB was directly mounted on the top of the reference sensor, in order to minimize out-of-axis acceleration effects. A Dytran accelerometer with sensitivity of  $0.1\text{V/g}$  and wide bandwidth of  $5\text{kHz}$  (with a max.  $\pm 2\%$  pass-band variation and a resonance frequency of



(a) SEM graphs of two fabricated accelerometers (b) AlN PE accelerometer testchip

Fig. 9. (a) SEM graphs of two fabricated accelerometer designs (left) backside of an annular diaphragm and (right) clamp-clamp beams. (b) Layout of the AlN PE accelerometer testchip. Besides the test structures that allow monitoring of the processing, a large and a small annular and a large and small quad-beam accelerometer structures are realized.

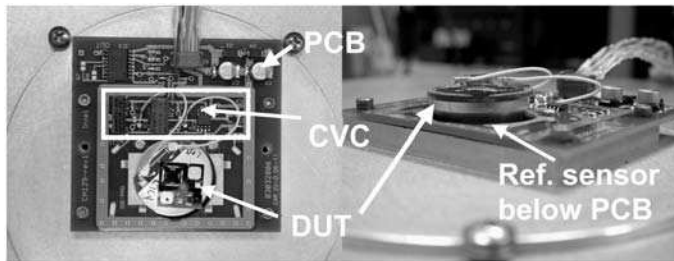


Fig. 10. Dynamic shaker setup.

$f_0=25\text{kHz}$ ) was used as a reference. Both the reference accelerometer and the shaker are set up such that the DUT on top of the reference is horizontally on the same level as the electronics PCB, see Fig. 10.

The overall optimization of the electronic sensor readout architecture and PCB design was focused on minimizing the electrical noise floor, which is imperative for testing these low noise accelerometers. Hence, the differential piezoelectric sensors are connected to the charge-to-voltage converters input (CVC) with two very short shielded low-capacitance coaxial cables in order to minimize noise coupling from the environment. Furthermore, the stiffness of the used coaxial cables and the way these cables are mounted between the sensor and the electronics is very important to obtain undistorted measurement results. Proper grounding of the electronics PCB and shaker setup is also mandatory in order to avoid ground loops and related 60Hz noise issues.

## 6.2 Low-noise PE accelerometer readout

PE MEMS accelerometers in the literature have noise floors as low as a few  $\mu\text{g}/\sqrt{\text{Hz}}$  e.g. (Wang et al., 2003; Levinzon, 2004; 2005). In almost all of these surface or bulk micromachined accelerometers, the total noise floor is dominated by electronic noise (of the 1st stage). Thus, in the following all dominant noise and error sources are reviewed and the impact on the overall acceleration noise density is calculated, in order to specify some hands-on design guidelines for the integrated CMOS readout solution to achieve actually

sub- $\mu\text{g}/\sqrt{\text{Hz}}$  levels (Gerfers, Ginsburg, Samara-Rubio, He, Manoli & Wang, 2007). The PE accelerometer mechanical-thermal noise and noise due to the losses in the PE material are given in (9) (Levinzon, 2004; Gerfers et al., 2007). A low-noise FET charge amplifier is used as a front-end stage to amplify the small transducer’s output charge signals. Thus, in order to detect an estimated noise floor of a few hundred  $\text{ng}/\sqrt{\text{Hz}}$  @ 10Hz all dominant noise sources have to be considered. In addition, the noise characteristics of the FET amplifier depends on the source impedance which is why the total noise floor of the PE accelerometer is determined by both noise characteristics of PE transducer and the FET amplifier (Levinzon, 2005). A simplified schematic of the front-end CVC shown in Fig. 11, which introduces three additional noise sources; a shot noise current density  $\bar{i}_{n,ota}$  (caused by the input bias current  $I_{GS}$  of the amplifier), a thermal and a  $1/f$  voltage noise source  $\bar{v}_{n,ota}$ . Referring these intrinsic amplifier noise sources to the sensor input, one obtains

$$\frac{\bar{a}_{n,ota}^2}{\Delta f} = \frac{\bar{i}_{n,ota}^2 |Z|^2}{V_s^2} = \frac{2qI_{GS}}{(\omega C_s)^2} \frac{C_s^2}{Q_{T,z}^2} \tag{7}$$

$$\frac{\bar{a}_{n,ota}^2}{\Delta f} \approx \left( \frac{\gamma_1 8kT}{3g_m} + \frac{\gamma_2 K_F I_{DS}}{f^{AF} C_{OX} L_{eff}^2} \right) \frac{C_s^2}{Q_{T,z}^2} \tag{8}$$

where  $I_{GS}$  denotes the amplifier input gate-source leakage current,  $\gamma_1, \gamma_2$  the noise excess factors,  $K_F$  the  $1/f$  transistor noise coefficient,  $I_{DS}$  the drain-source bias current of the input devices,  $AF$  the  $1/f$  noise slope coefficient,  $C_{OX}$  the gate oxide capacitance and  $L_{eff}$  the effective drawn transistor length. Please note, that the sensor capacitance is significantly larger than the integrator capacitance in order to obtain the required CVC gain. The lower bound for  $C_{int}$  is given by the full scale sensor signal and the maximum signal swing of the first CVC stage whereas the upper bound of  $C_{int}$  is given by the dynamic range requirements. The penalty of the 2nd stage amplifier on the overall noise floor is rather small, since it is divided by the first stage gain. The differential CVC was built from a pair of ultra low-leakage current low-noise single-ended JFET amplifiers featuring a voltage noise floor ( $\bar{v}_{n,ota}$ ) as low as  $5\text{nV}/\sqrt{\text{Hz}}$  and simultaneously an extremely low current noise of  $1\text{fA}/\sqrt{\text{Hz}}$ . For an expected sensor capacitance of  $C_s = 500\text{pF}$  and a sensitivity of  $Q_{T,z} = 5.2\text{pC/g}$ , the equivalent acceleration noise floor ( $\bar{a}_{n,ota}$ ) is  $670\text{ng}/\sqrt{\text{Hz}}$ . The expected sensor Brownian noise floor is around  $10\text{ng}/\sqrt{\text{Hz}}$ , which is still much lower than the detectable noise floor, limited by interface readout electronics.

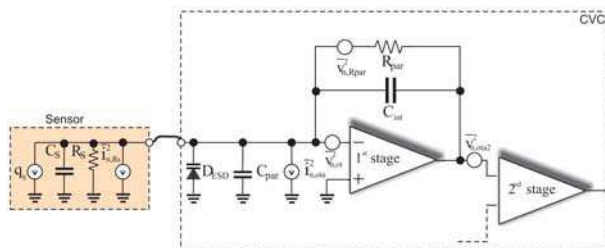


Fig. 11. PE MEMS sensor readout architecture. All dominant noise and error sources of the charge amplifier configuration are illustrated.

### 6.3 Measurements and characterizations

The formerly presented accelerometer structures have been analyzed in detail theoretically and numerically. Static and modal simulations with Finite Element Analysis (FEA) simulator are done to analyze the mechanical response given in at different applied accelerations. The symmetric quad-beam structure and the annular beam structure were fabricated using CMOS compatible piezoelectric AlN thin films and silicon-on-insulator (SOI) wafers using different proof mass weights and SOI thickness ranging from 7.75 – 12 $\mu\text{m}$  (Gerfers et al., 2006). The complete layout of the different accelerometers and process monitor structures is shown in Fig. 9(b).

The measured dynamic charge responses for two annular accelerometers with 8.6 and 12 $\mu\text{m}$  silicon beam thickness are shown in Fig. 12(a). The quality factor of these devices equals  $Q = 290$ . Figure 12(b) presents the total noise floor of the accelerometer plus interface electronics. The tested accelerometer sensitivities range from 0.06 to 1.73pC/g with acceleration noise floors from 0.8 to 17 $\mu\text{g}/\sqrt{\text{Hz}}$ . The complete test results of two high performance accelerometers; the large annular design (LC) and the large quad-beam structure (LS) both with 7.75 $\mu\text{m}$  thick SOI beams is given in Tab. 2. Obviously, the simulated FEA values match well with the measured values validating our design methodology for future projects. Although, in order to meet the stringent specifications of condition-based maintenance and vibration monitoring the accelerometer performance has to be further improved especially in terms of signal-to-noise ratio.

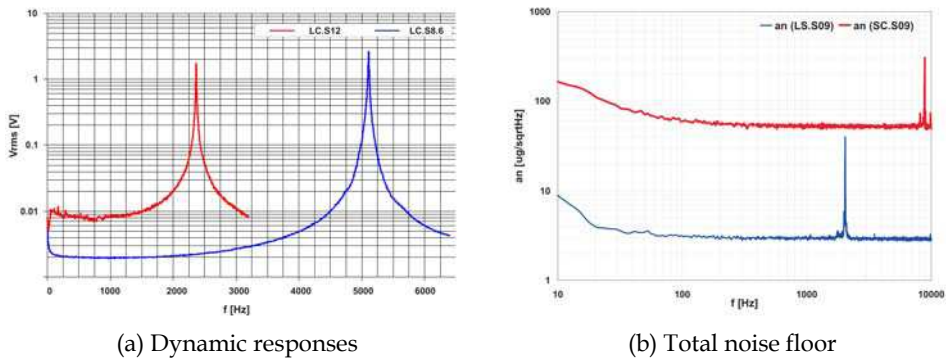


Fig. 12. (a) Measured dynamic charge responses for two annular accelerometers with 8.6 and 12 $\mu\text{m}$  silicon beam thickness. The quality factor of this device equals  $Q = 290$ . (b) Measured total noise floor spectrum of the accelerometer plus interface electronics.

		LC, 7.75 $\mu\text{m}$ SOI		LS, 7.75 $\mu\text{m}$ SOI	
		FEA	Meas.	FEA	Meas.
$f_0$	[kHz]	5.5	5.3	1.3	1.8
Sensitivity	[pC/g]	0.27	0.22	1.77	1.73
Sensor Capacitance	[pF]		110		195
Size (Area)	[mm <sup>2</sup> ]		20		36
Proof mass	[mgram]		4.39		4.37

Table 2. Measured and FEA-simulated sensitivities of the two high performance accelerometers, the large annular design (LC) and the large quad-beam structure (LS) both with 7.75 $\mu\text{m}$  thick SOI beams.

## 7. Optimized AIN piezoelectric accelerometer

In the following, a new accelerometer design accomplishing an optimized performance in terms of charge sensitivity per unit area is introduced. Besides the dynamic range improvement we further introduce a sensing structure, which shifts higher order resonance modes to higher frequencies without affecting the charge sensitivity and fundamental resonance.

### 7.1 Review of the piezoelectric accelerometer noise performance

The total noise of a piezoelectric sensor in terms of equivalent acceleration noise is described in (9)-(10), which consists of two noise sources: mechanical-thermal or Brownian noise ( $\bar{a}_{n,mech}^2$ ) and electrical-thermal noise ( $\bar{a}_{n,ele}^2$ ),

$$\frac{\bar{a}_{n,tot}^2}{\Delta f} = \frac{\bar{a}_{n,mech}^2}{\Delta f} + \frac{\bar{a}_{n,ele}^2}{\Delta f} \quad (9)$$

$$\frac{\bar{a}_{n,tot}^2}{\Delta f} = 4k_B T \left( \frac{\omega_0}{mQ} + \frac{\eta C_S}{\omega Q_{T,\vec{z}}} \right) \quad (10)$$

where  $k_B$ ,  $T$ ,  $\omega_0$ ,  $m$ ,  $Q$  are Boltzmann's constant, absolute temperature, resonant frequency, effective sensor mass, quality factor; and  $C_S$ ,  $\eta$ ,  $\omega$ ,  $Q_{T,\vec{z}}$  are the sensor capacitance, dissipation factor of the piezoelectric material, operating frequency, and longitudinal sensitivity, respectively. Thus, the noise spectrum is dominated by Brownian noise at high frequencies and by electrical-thermal noise at low frequencies since  $\bar{a}_{n,ele}^2$  has a  $1/f$  relation.

As mentioned before, vibration condition monitoring requires a very low noise floor at low frequency because very little vibration amplitude in terms of acceleration is produced at low frequency. Therefore, reducing the electrical-thermal noise  $\bar{a}_{n,ele}^2$  is our objective. According to (10) to minimize  $\bar{a}_{n,ele}^2$ , one strategy would be to increase the charge sensitivity  $Q_{T,\vec{z}}$  and maintain or even reduce at the same time  $C_S$  and  $\eta$ . The charge sensitivity of the piezoelectric accelerometer based on the bending mode is described by

$$Q_{T,\vec{z}} = \int_{\text{Electrode Area}} (d_{31} \times \sigma) dA. \quad (11)$$

But from this relation it is obvious that for a given piezoelectric material (i.e.  $d_{31}$  is determined) and given electrode area, the charge sensitivity, the accelerometer capacitance as well as the dielectric loss are constrained. As a result, increasing the charge sensitivity with an improved sensing structure is the main design objective outlined in the following.

### 7.2 SNR optimized piezoelectric accelerometer structure

Maximizing the accelerometer charge sensitivity and therewith the overall sensor signal-to-noise ratio has been accomplished by revising the original beam structure (illustrated in Fig. 15) used in the initial studies (Wang et al., 2003; Gerfers et al., 2006). By remodeling the rectangular beam shape into a trapezoidal beam shape structure, an applied external force causes stress that is concentrated on a smaller active PE area. This way, a higher stress

magnitude is obtained on a smaller electrode area accomplishing both design tasks in terms of increasing the charge sensitivity  $Q_{T,\bar{z}}$  and reducing the total PE electrode area. Furthermore, as a result of the reduced active PE area, both the sensor capacitance  $C_S$  as well as the accelerometer dissipation factor  $\eta$  are reduced as well. Figure 13 illustrates four different sensor designs exploring the concept of stress concentration. All sensing structures are designed to have the same resonance frequency and weight of the proof mass for fair comparison. Their sensitivities have been analyzed by FEA simulation, which are plotted as functions of the electrode area in Fig. 14.

Compared to the original designs I and II introduced in Sec. 6, which are using the conventional trampoline and the annular diaphragm sensing structure, device III and IV clearly show an improved charge sensitivity because the tapered-beam design results in higher stress concentration on the electrode area. As a result, the new devices permit to use smallest die size due to its distinguished area utilization. Moreover, Fig. 14 features a relative linear relationship between the charge sensitivity  $Q_{T,\bar{z}}$  and the electrode area for designs I and II, whereas sensor structures III and IV reveal a point of maximum sensitivity per area due to the non-linear slope of  $Q_{T,\bar{z}}$ . This optimal point can be found by calculating the derivative of  $(\partial Q_{T,\bar{z}})/(\partial A)$  and is obtained for an electrode area of  $3.5\text{mm}^2$ .

Besides redesigning the beam structure in order to improve the overall signal-to-noise ratio, additional effort was spent reducing the transversal sensitivities  $Q_{T,\bar{x}}$  and  $Q_{T,\bar{y}}$ . FEA simulations prove that structure IV is less susceptible to transversal accelerations than device III. In addition, by introducing four balanced bars designed to connect the four sensing beams at node positions, as illustrated in Fig. 14(a), the whole structure is even more reliable and is stiffer in the X-Y directions (minimizing the transversal sensitivity) without impairing the resonance frequency and sensitivity. This can be visually confirmed by analyzing the stress contours of the structure with balanced bars given in Fig. 14(a).

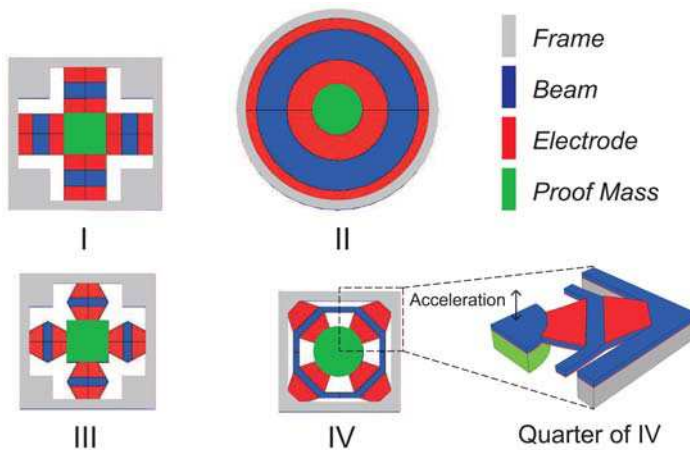
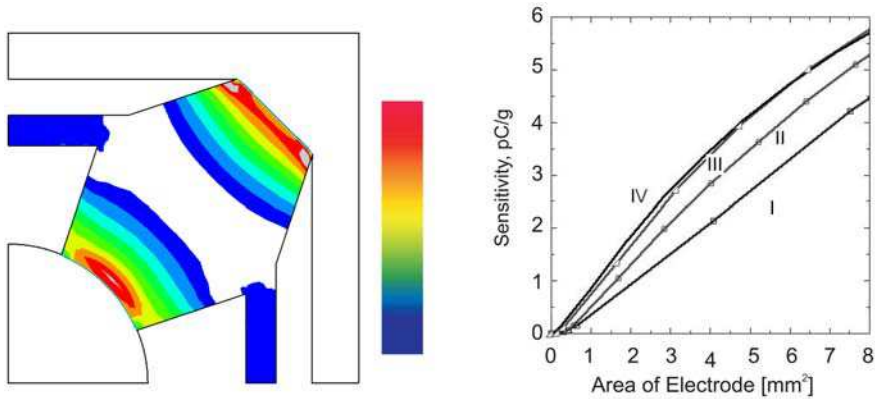


Fig. 13. Different sensing structures were investigated to have optimized performance. They are designed to have same resonance frequency and weight of the the proof mass for fair comparisons. Design I and II use conventional beam and membrane structures, while device III and IV employ a tapered-beams design.



(a) Stress contours of design IV beams (b) Simulated charge sensitivities per unit area

Fig. 14. (a) Stress contours of design IV with balanced bars, which connect the sensing beams at the node positions (zero stress point) to provide better stability and less off-axis sensitivity. (b) FEA simulated charge sensitivities per unit area.

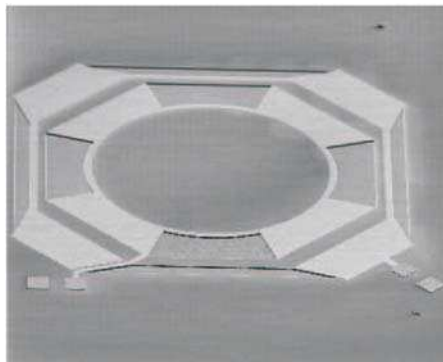
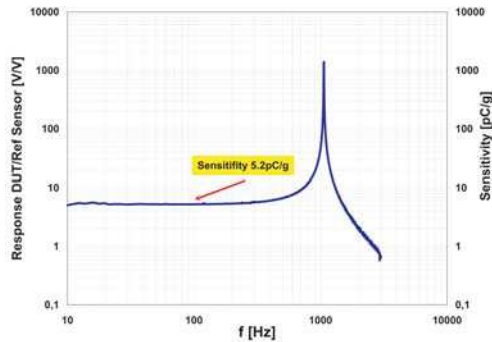


Fig. 15. SEM micrograph of design IV front-side before DRIE processing.

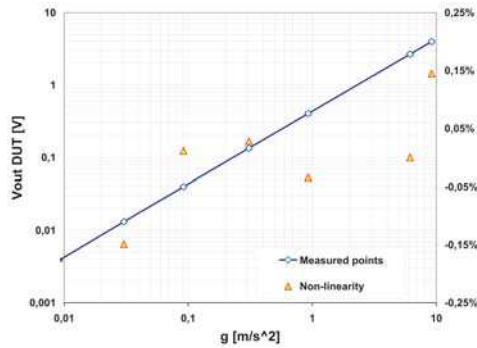
### 7.3 Experimental results

The dynamic frequency responses of the accelerometers were measured using mechanical shaker in an open-loop setup as shown in Fig. 10. The tested output spectra of PE accelerometer is shown in Fig. 16(a). The mean of the tested charge sensitivity for design IV is  $5.2 \text{ pC/g}$  with a  $Q$  of 160 (Gerfers, Bar, Northemann, Manoli, Kohlstadt & Wang, 2007). The measured sensor linearity from  $1 \text{ mg}$  to  $10 \text{ g}$  of design IV is shown in Fig. 16(b) with maximum deviation of less than 0.3% over the entire  $g$ -range. The lower measurement limit was given by the power amplifier of the shaker, while the upper level is restricted by the chosen CVC gain and output voltage swing. Measurements with a reduced CVC gain show reliable operation beyond  $20 \text{ g}$  acceleration amplitudes. The measured noise spectrum, shown in Fig. 16(c), demonstrates a total wideband noise floor of  $670 \text{ ng}/\sqrt{\text{Hz}}$ . The low frequency noise ( $1/f$  noise) equals  $4.2 \text{ g}/\sqrt{\text{Hz}} @ 10 \text{ Hz}$  such that the noise corner frequency is below  $100 \text{ Hz}$  (Gerfers, Ginsburg, Samara-Rubio, He, Manoli & Wang, 2007). Please note, that

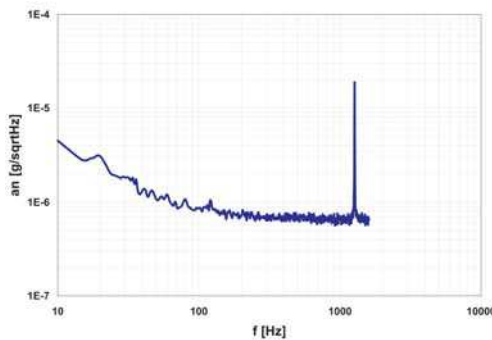
the low frequency noise slope is less than  $f^{-1}$ . The spread of the measured accelerometer capacitance  $C_s$  is within 2.5% ( $3\sigma$ ) and the dissipation factor  $\eta = 1/(2 f C_s R_p)$  is 0.11% @ 230Hz. The performance of the proposed accelerometer design IV is summarized in Table 3.



(a) Dynamic frequency response of design IV



(b) Linearity of design IV



(c) Noise spectrum

Fig. 16. (a) Measured frequency response of the design IV PE AlN accelerometer. (b) Measured linearity showing less than 0.3% deviation from 0.01 – 10g acceleration level. (c) measured total noise floor spectrum of sensor and interface electronics.

		Design IV
$f_0$	[kHz]	1.1
Sensitivity	[pC/g]	5.2
Sensor Capacitance	[pF]	500
Dissipation factor	[1]	0.11%
Sensor Size	[mm <sup>2</sup> ]	45.8
Proof mass	[mgram]	10.1

Table 3. Device parameter summary.

## 8. Conclusion

Polycrystalline AlN films were prepared by reactive sputtering; optimized piezoelectric and crystalline properties were obtained at right sputtering conditions. Two types of piezoelectric MEMS devices, surface-micromachined resonators and bulk-micromachined accelerometers, utilizing longitudinal ( $d_{33}$  mode) and transverse ( $d_{31}$  mode) piezoelectric effects were fabricated and characterized.

We demonstrate a unique approach to integrating multiple-frequency FBARs in a single chip. By controlling in-plane dimensions of the periodic tuning patterns, resonance frequencies of modified FBARs are modulated corresponding to the mass loading percentages. As a result, multiple-frequency FBARs can be lithographically defined by a single deposition/patterning processing sequence. To obtain a desirable frequency response, a pure frequency shift, the pitch of the tuning patterns needs to be smaller than the membrane thickness. This approach provides a potential solution for integrating multiple-frequency FBAR filters of adjacent bands or frequency trimming. The fabricated piezoelectric resonators achieve a  $Q$  of 1000 and an electromechanical coupling of 6.5% at 2GHz. The effective coupling coefficient  $k_t^2$  for all frequency-tuned FBARs, was maintained within 90% of the non-modified one.

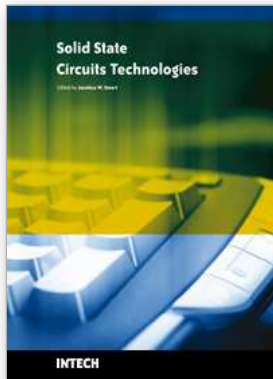
Vibration condition monitoring requires a very low acceleration noise floor at low frequency in order to be able to detect small acceleration amplitudes. In this chapter we have presented a new sensing structure for piezoelectric accelerometers improving the overall signal-to-noise ratio such that the fabricated accelerometers fulfill the vibration condition monitoring requirements. The devices take advantage of tapered beams resulting in stress concentration on the electrode area. As a result, the accelerometer charge sensitivity increases while at the same time both the sensor capacitance and the dissipation factor can be reduced therewith improving the electrical-thermal acceleration noise. Thus, the novel sensing structure features smallest die size due to its distinguished area utilization. The sensing structure has been designed to have low transverse sensitivity and to be reliable introducing four balanced bars designed to connect the four sensing beams at node positions therefore, the whole structure is stiffer in the X-Y direction but without impairing the resonance frequency and charge sensitivity.

Experimental results confirm the significantly improved sensitivity of the accelerometers obtained with the proposed sensing structures. The tested charge sensitivity is 5.2pC/g and the measured total noise floor of sensor plus interface electronics is as low as 670ng/ $\sqrt{\text{Hz}}$ .

## 9. References

- Gerfers, F., Bar, H., Northemann, T., Manoli, Y., Kohlstadt, M. & Wang, L.-P. (2007). An Ultra Low-Noise Vibration Monitoring System, *IEEE Sensors Conf.* pp. 880–883.
- Gerfers, F., Ginsburg, E., Samara-Rubio, D., He, M. Y., Manoli, Y. & Wang, L.-P. (2006). Fabrication and Characterization of Bulk-micromachined Accelerometers Based on AlN Piezoelectric Sensing and SOI Wafers, *20th Eurosensors* pp. –.
- Gerfers, F., Ginsburg, E., Samara-Rubio, D., He, M., Manoli, Y., & Wang, L.-P. (2007). Sub- $\mu\text{g}$  Ultra Low Noise MEMS Accelerometers based on CMOS-Compatible Piezoelectric AlN Thin Films, *Int. Conf. on Solid-State Sensors, Actuators and Microsystems* pp. 1191–1194.
- Giacovazzo, C. (ed.) (2002). *Fundamentals of crystallography*, Oxford University Press.
- Huang, Z., Suo, Z., Wang, L.-P., Shim, D. & Ma, Q. (2005). A Novel Approach to Integrate Multiple Film Bulk Acoustic Resonators (FBAR) with Different Frequencies in A Single Chip, *Proc. of Nano Science and Technology Institute (NSTI) Nanotechnology Conf.*, Vol. 3, pp. 435–438.
- Kulah, H., Chae, J., Yazdi, N. & Najafi, K. (2006). Noise Analysis and Characterization of a SD Capacitive Microaccelerometer, *IEEE J. Solid-State Circuits* 41(2): 352–361.
- Lakin, K. M., Kline, G. R., & McCarron, K. T. (1995). Development of Miniature Filters for Wireless Applications, *IEEE Trans. Microw. Theory Tech.* 43(12): 2933–2939.
- Lakin, K.M., McCarron, K. T. & McDonald, J. (2000). Temperature Compensated Bulk Acoustic Thin Film Resonators, *Proc. IEEE Ultrasonics Symposium*, pp. 855–858.
- Levinzon, F. A. (2004). Fundamental noise limit of piezoelectric accelerometer, *IEEE Sensors J.* 4(1): 108 – 111.
- Levinzon, F. A. (2005). Noise of piezoelectric accelerometer with integral FET amplifier, *IEEE Sensors Conf.* pp. 1235 – 1242.
- Liaw, H. M. & Hickernell, F. S. (1995). Characterization of Sputtered Polycrystalline Aluminum Nitride on Silicon by Surface Acoustic Wave Measurements, *IEEE Trans. Ultrason., Ferroelectr., Freq. Control* 42(2): 404.
- Loebl, H. P., Klee, M., Kiewitt, O.W. R., Dekker, R. & Pelt, E. V. (1999). Piezo-electric AlN and PZT Films for micro-electronic Applications, *IEEE Ultrasonics Symposium*, pp. 1031–1036.
- McLean, C. & Wolfe, D. (2002). Intelligent Wireless Condition-Based Maintenance. (Machine Monitoring/Networking)., *Sensors Magazine* 19(6): 14–17.
- Monajemi, P. & Ayazi, F. (2006). Design Optimization and Implementation of a Microgravity Ccapacitive HARPSS Accelerometer, *IEEE J. Solid-State Circuits* 41(6): 39–46.
- Naik, R. S., Lutsky, J. J., Reif, R. & Sodini, C. (2000). Measurements of the Bulk, C-axis Electromechanical Couplingconstant as a Function of AlN Film Quality, *IEEE Trans. Ultrason., Ferroelectr., Freq. Control* 47: 292.
- Nye, J. F. (1995). *Physical Properties of Crystals: Their Representation by Tensors and Matrices*, Oxford University Press.
- Oestman, K. B., Sipil, S. T., Uzunov, I. S. & Tchamov, N. T. (2006). Novel VCO Architecture Using Series Above-IC FBAR and Parallel LC Resonance, *IEEE J. Solid-State Circuits* 41(1): 2248–2246.

- Piazza, G., Stephanou, P. J., Black, J. P., White, R. M. & Pisano, A. P. (2005). Single-chip multiple-frequency RF microresonators based on aluminum nitride contour-mode and FBAR technologies, *IEEE Ultrasonics Symposium*, Vol. 2, pp. 1187–1190.
- Ruby, R., Bradley, P., Oshmyansky, Y. & Chien, A. (2001). Thin Film Bulk Acoustic Resonators (FBAR) for Wireless Applications, *IEEE Ultrasonics Symposium*, pp. 813–821.
- Ruby, R. & Merchant, P. (1994). Micromachined Thin Film Bulk Acoustic Resonators, *IEEE Frequency Control Symposium* pp. 135–138.
- Setter, N. (2005). *Electroceraic-based MEMS: fabrication-technology and applications*, Springer.
- Trolier-McKinstry, S. & Murali, P. (2004). Thin Film Piezoelectrics for MEMS, *Kluwer, Journal of Electroceramics*, pp. 7–17.
- Ueda, M., Nishihara, T., Tsutsumi, J., Taniguchi, S., Yokoyama, T., Inoue, S., Miyashita, T. & Satoh, Y. (2005). High-Q Resonators using FBAR/SAW Technology and their Applications, *IEEE Int. Microwave Symposium Digest*, pp. 209–212.
- Wang, L.-P., Ginsburg, E., Diamant, D., Ma, Q., Huang, Z. & Suo, Z. (2006). Method to Fabricating Multiple-Frequency Film Bulk Acoustic Resonators in a Single Chips, *IEEE Int. Frequency Control Symposium and Exposition*, pp. 793–796.
- Wang, L.-P., Wolf, R., Yu, W., Deng, K., Zou, L., Davis, R. & Trolier-McKinstry, S. (2003). Design, Fabrication, and Measurement of High-Sensitivity Piezoelectric Microelectromechanical Systems Accelerometers, *J. Microelectromech. Syst.* 4(12): 433 – 439.
- Weigel, R., Morgan, D. P., Owens, J. M., Ballato, A., Lakin, K. M., Hashimoto, K. & Ruppel, C. W. (2002). Microwave Acoustic Materials, Devices, and Applications, *IEEE Microwave Acoustic Materials, Devices, and Applications* 50(3): 738–749.
- Xu, F., Wolf, R. A., Yoshimura, T. & Trolier-McKinstry, S. (2002). Piezoelectric Films for MEMS Applications, *Proc. IEEE 11th International Symposium on Electrets*, pp. 386–396.



## **Solid State Circuits Technologies**

Edited by Jacobus W. Swart

ISBN 978-953-307-045-2

Hard cover, 462 pages

**Publisher** InTech

**Published online** 01, January, 2010

**Published in print edition** January, 2010

The evolution of solid-state circuit technology has a long history within a relatively short period of time. This technology has led to the modern information society that connects us and tools, a large market, and many types of products and applications. The solid-state circuit technology continuously evolves via breakthroughs and improvements every year. This book is devoted to review and present novel approaches for some of the main issues involved in this exciting and vigorous technology. The book is composed of 22 chapters, written by authors coming from 30 different institutions located in 12 different countries throughout the Americas, Asia and Europe. Thus, reflecting the wide international contribution to the book. The broad range of subjects presented in the book offers a general overview of the main issues in modern solid-state circuit technology. Furthermore, the book offers an in depth analysis on specific subjects for specialists. We believe the book is of great scientific and educational value for many readers. I am profoundly indebted to the support provided by all of those involved in the work. First and foremost I would like to acknowledge and thank the authors who worked hard and generously agreed to share their results and knowledge. Second I would like to express my gratitude to the InTech team that invited me to edit the book and give me their full support and a fruitful experience while working together to combine this book.

### **How to reference**

In order to correctly reference this scholarly work, feel free to copy and paste the following:

Friedel Gerfers, Peter M. Kohlstadt, Eyal Ginsburg, Ming Yuan He, Dean Samara-Rubio, Yiannos Manoli and Li-Peng Wang (2010). Sputtered AlN Thin Films for Piezoelectric MEMS Devices - FBAR Resonators and Accelerometers, Solid State Circuits Technologies, Jacobus W. Swart (Ed.), ISBN: 978-953-307-045-2, InTech, Available from: <http://www.intechopen.com/books/solid-state-circuits-technologies/sputtered-aln-thin-films-for-piezoelectric-mems-devices-fbar-resonators-and-accelerometers>

**INTECH**  
open science | open minds

### **InTech Europe**

University Campus STeP Ri  
Slavka Krautzeka 83/A  
51000 Rijeka, Croatia  
Phone: +385 (51) 770 447  
Fax: +385 (51) 686 166

### **InTech China**

Unit 405, Office Block, Hotel Equatorial Shanghai  
No.65, Yan An Road (West), Shanghai, 200040, China  
中国上海市延安西路65号上海国际贵都大饭店办公楼405单元  
Phone: +86-21-62489820  
Fax: +86-21-62489821



© 2010 The Author(s). Licensee IntechOpen. This chapter is distributed under the terms of the [Creative Commons Attribution-NonCommercial-ShareAlike-3.0 License](#), which permits use, distribution and reproduction for non-commercial purposes, provided the original is properly cited and derivative works building on this content are distributed under the same license.